Petroleum Science 21 (2024) 3142–3156

Contents lists available at ScienceDirect

Petroleum Science

journal homepage: www.keaipublishing.com/en/journals/petroleum-science

Original Paper

Extraction of reflected waves from acoustic logging data using variation mode decomposition and curvelet transform

Fan-Tong Kong [a], Yong-Xiang Liu [a], Xi-Hao Gu [b], Li Zhen [c], Cheng-Ming Luo [a], Sheng-Qing Li [b, *]

[a] Ocean College, Jiangsu University of Science and Technology, Zhenjiang, 212100, Jiangsu, China
[b] School of Geosciences, China University of Petroleum (East China), Qingdao, 266580, Shandong, China
[c] State Key Laboratory of Oil and Gas Reservoir Geology and Exploitation, Chengdu University of Technology, Chengdu, 610059, Sichuan, China

ARTICLE INFO

Article history:
Received 8 November 2023
Received in revised form
10 April 2024
Accepted 22 May 2024
Available online 24 May 2024

Edited by Meng-Jiao Zhou

Keywords:
Borehole acoustic reflection imaging
Variation mode decomposition
Curvelet transform
Weak signal extraction

ABSTRACT

Remote reflection waves, essential for acquiring high-resolution images of geological structures beyond boreholes, often suffer contamination from strong direct mode waves propagating along the borehole. Consequently, the extraction of weak reflected waves becomes pivotal for optimizing migration image quality. This paper introduces a novel approach to extracting reflected waves by sequentially operating in the spatial frequency and curvelet domains. Using variation mode decomposition (VMD), single-channel spatial domain signals within the common offset gather are iteratively decomposed into high-wavenumber and low-wavenumber intrinsic mode functions (IMFs). The low-wavenumber IMF is then subtracted from the overall waveform to attenuate direct mode waves. Subsequently, the curvelet transform is employed to segregate upgoing and downgoing reflected waves within the filtered curvelet domain. As a result, direct mode waves are substantially suppressed, while the integrity of reflected waves is fully preserved. The efficacy of this approach is validated through processing synthetic and field data, underscoring its potential as a robust extraction technique.

1. Introduction

Borehole acoustic reflection imaging technology involves utilizing the recorded secondary arrival, referred to as the reflected signal induced by the interaction between energy radiated away from the borehole and outside geological structures. This technology generates high-resolution images for formations tens of meters away from the borehole (Che et al., 2014; Wei and Tang, 2012). Notably, borehole shear-waves reflection imaging offers natural azimuthal sensitivity and deeper detection depth, owing to its utilization of low extraction frequencies (Li et al., 2021; Wang et al., 2020). This technology has emerged as a pivotal tool for various applications, including fracture identification (Zhang et al., 2015), near-borehole fault analysis (Lee et al., 2019), adjacent borehole detection (Cheng et al., 2023; Gu et al., 2021), and hydraulic fracturing evaluation (Hei et al., 2023).

Despite the significance of the reflected waves, the measured acoustic logging waveform is often dominated by the overwhelming direct mode waves that propagate along the borehole boundary (Tao et al., 2008a). When a monopole source is employed, most of the energy is confined in the fluid-filled borehole as P-waves, S-waves, Stoneley waves, and pseudo-Rayleigh waves. Only less than 1% of energy leaks into the formation as body waves that can be reflected and received (Wang et al., 2015). Furthermore, the body waves are considerably attenuated when traveling in the outside formation, rendering the extraction of reflected waves arduous. Even the dipole source has the ability to generate the large amplitude reflected SH-waves (Li et al., 2017b, 2022), however, which is significantly contaminated by the direct dispersive flexure waves. Consequently, the extraction of the reflected waves becomes a crucial pre-processing step, garnering considerable attention from researchers.

Various approaches have been proposed for this purpose. Parameter prediction methods simulate the f-k (frequency-wavenumber) spectrum of the direct mode waves based on a preset propagation model and then subtract them from the total f-k spectrum (Tang, 1997; Hirabayashi and Leaney, 2019). The results of

* Corresponding author.
E-mail address: shidalishengqing@yeah.net (S.-Q. Li).

https://doi.org/10.1016/j.petsci.2024.05.017

these methods heavily rely on the given velocity and attenuation models, which are often challenging to estimate. The median filter, based on statistical theory, is useful and rapid, but it can produce irregular results (Li et al., 2002). The Karhunen-Loève transform decomposes the total waveform into several components using statistical analysis (Li et al., 2017a), and the direct waves could be reconstructed by the most dominant components, under the hypothesis that most energy comes from direct waves. The f-k transform is a simple yet important method to extract the reflected waves (Hornby, 1989), relying on the apparent velocity difference between direct and reflected events. Retaining additional time information by transforming the logging waveform into the slowness-time domain, the high-resolution radon transform yields improved extraction results (Li and Yue, 2017). Employing both time and frequency information, Tao et al. (2008b) proposed soft threshold strategies to separate the reflected waves using the dual-tree complex wavelet transform. This approach is run on the common shot gather and is time-consuming, heavily dependent on set super-parameters. Leveraging shear and scale information, the shearlet transform can more accurately identify and extract reflected signals (Chen et al., 2019). Moreover, this method is performed on the common offset gather (COG), significantly improving efficiency.

It is evident from the aforementioned methods that direct and reflected events significantly differ in terms of wavenumber (spatial frequency), energy, scale, and orientation. In this paper, we leverage these distinctive characteristics to extract reflected waves from COG data. We employ a variation mode decomposition (VMD) in the spatial frequency domain, decomposing the data into two modes. We then subtract the low-wavenumber mode, which predominantly contains direct events, from the full waveform. The high-energy direct mode waves are subsequently eliminated using a hard threshold applied to the curvelet coefficients. Finally, the upgoing and downgoing reflected waves are disentangled using the inverse curvelet transform applied to selected curvelet coefficients corresponding to specific scales and orientations. We validate the effectiveness of the proposed method using both synthetic and field data.

2. Methodology

2.1. Variation mode decomposition

To address the issue of mode mixing in empirical mode decomposition (EMD) (Huang et al., 1998), VMD was introduced as an alternative by Dragomiretskiy and Zosso (2014). VMD presents robust noise resistance and stronger mathematical underpinnings. It concurrently decomposes a single-channel input signal into a set of band-limited intrinsic mode functions (IMFs, also denoted as modes) at distinct center frequencies. VMD has found applications in various seismic contexts, including seismic denoising (Yu and Ma, 2018), ground-roll attenuation (Liu et al., 2022), and time-frequency analysis (Liu et al., 2016).

Given the acoustic logging array waveform $\boldsymbol{W}(o,t.x)$, where o denotes the offset (receiver index), a typical COG can be derived as $\boldsymbol{D}_o(t,x)$, represented as an $M \times N$ matrix $\boldsymbol{D} = [d_1, d_2, \cdots, d_N]$, where M and N correspond to the sampling points of the measured depth x and recording time t, respectively. The vector $\boldsymbol{d}_n = (\boldsymbol{D}_{n1}, \boldsymbol{D}_{n2}, \cdots, \boldsymbol{D}_{nM}), (n = 1, 2, \cdots, N)$ signifies the recording data at a specific time point, akin to a single-channel spatial domain signal $d(x)$.

When fed a single-channel signal $d(x)$, VMD yields an ensemble of IMFs $u_g(x)$ under the constraint that their summation reconstructs the input signal $d(x)$:

$$d(x) = \sum_G u_g(x), \tag{1}$$

where $\sum_G := \sum_{g=1}^{G}$ represents the summation over all modes, with the total number of modes G determined by preset hyper-parameters. The paper adopts $G = 2$. IMFs are defined as amplitude-modulated-frequency-modulated signals:

$$u_g(x) = a_g(x)cos\left(\varphi_g(x)\right), \tag{2}$$

where $a_g(x)$ and $\varphi_g(x)$ denote the amplitude and phase functions of the gth mode, respectively.

Mode decomposition is executed by solving a constrained variational problem, with the objective function as follows:

$$\begin{aligned} &\min_{\{u_g\},\{k_g\}} \left\{ \sum_G \left\| \partial_x \left[\left(\delta(x) + \frac{i}{\pi x} \right) * u_g(x) \right] e^{-ik_g x} \right\|_2^2 \right\} \\ &\text{s.t.} \sum_G u_g(x) = d(x), \end{aligned} \tag{3}$$

where k_g represents the set of all central spatial frequencies of $u_g(x)$ modes, and $\delta(x)$ signifies the Dirac function. By introducing a quadratic penalty term and Lagrange multipliers $\lambda(x)$, the constrained variational problem is reformulated into an unconstrained optimization problem:

$$\begin{aligned} L(\{u_g\},\{k_g\},\lambda) = \alpha \sum_G \left\| \partial_x \left[\left(\delta(x) + \frac{i}{\pi x} \right) * u_g(x) \right] e^{-ik_g x} \right\|_2^2 \\ + \left\| d(x) - \sum_G u_g(x) \right\|_2^2 + \langle \lambda(x), d(x) - \sum_G u_g(x) \rangle \end{aligned} \tag{4}$$

where α signifies the balance weight for the data-fidelity term, and * denotes convolution. The alternating direction method of multipliers (ADMM) (Rockafellar, 1973) is employed to iteratively solve the optimization problem in the spatial frequency domain, as depicted in Algorithm 1.

The symbols $\widehat{\ }$ in Algorithm 1 represent the Fourier transforms. The optimization process is terminated when the relative difference in the total modes between two consecutive iterations becomes smaller than the predefined tolerance value ϵ. As indicated in Eq. (8), the modes in the spatial domain are obtained by taking the real part $\Re$ of the inverse Fourier transform of the calculated $\widehat{u}_g(k)$.

Algorithm 1. ADMM optimization for VMD

Require: $\left\{\hat{u}_g^1\right\},\left\{\hat{k}_g^1\right\},\hat{\lambda}^1,n\leftarrow 0,\varepsilon\leftarrow 5\mathrm{e}^{-3},\alpha=1\mathrm{e}^3,\tau=0.01$

repeat

$n\leftarrow n+1$

for $g=1:G$ **do**

Update the gth mode $\hat{u}_g$ for all $k\geq 0$:

$$\hat{u}_g^{n+1}(k)\leftarrow\frac{\hat{d}(k)-\sum_{i<g}\hat{u}_i^{n+1}(k)-\sum_{i>k}\hat{u}_i^n(k)+\frac{\hat{\lambda}^n(k)}{2}}{1+2\alpha(k-k_g^n)^2} \tag{5}$$

Update the center spatial frequency k_g:

$$k_g^{n+1}\leftarrow\frac{\int_0^\infty k\|\hat{u}_g^{n+1}(k)\|^2\mathrm{d}k}{\int_0^\infty\|\hat{u}_g^{n+1}(k)\|^2\mathrm{d}k} \tag{6}$$

end for

Dual ascent for all $k\geq 0$:

$$\hat{\lambda}^{n+1}(k)\leftarrow\hat{\lambda}^n(k)+\tau\left(\hat{d}(k)-\sum_G\hat{u}_g^{n+1}(k)\right) \tag{7}$$

until convergence: $\sum_G\left\|\hat{u}_g^{n+1}-\hat{u}_g^n\right\|_2^2/\left\|\hat{u}_g^n\right\|_2^2<f$

for $g=1:G$ **do**

$$u_g(x)=\Re(F^{-1}(\hat{u}_g(k))) \tag{8}$$

end for

return Decomposed modes in spatial domain: $u_g(x),g=1,2,...,G$

2.2. Curvelet transform

The curvelet transform, an amalgamation of principles from wavelet and ridgelet transforms, extends its prowess by discerning curved and smooth attributes within data, showcasing its distinct efficacy in scenarios where conventional transforms exhibit limitations (Ma and Plonka, 2010). As a sophisticated mathematical tool, the curvelet transform has garnered prominence in the image and seismic data analysis (Song et al., 2023; Starck et al., 2002), revered for its exceptional aptitude in capturing intricate and anisotropic patterns innate to such signals.

Rooted in the concepts of multiscale analysis and directional decomposition, the curvelet transform encapsulates a sparse representation framework. Herein, the input 2D common offset gather signals find approximation through a summation of scaled and rotated curvelet functions $\psi_{j,l,\boldsymbol{S}}(t,d)$, weighted by corresponding coefficients $c_{j,l,S}$:

$$\boldsymbol{D}(t,x)\approx\sum_{j,l,S}c_{j,l,\boldsymbol{S}}\psi_{j,l,\boldsymbol{S}}(t,x). \tag{9}$$

In contrast to wavelets, curvelet $\psi_{j,l,\boldsymbol{S}}$ encompasses a triple index: 1) scale $2^{-j},j=1,2,\ldots,J$; 2) equi-spaced sequence of rotation angles $\theta_l=2\pi l\cdot 2^{-\lfloor j/2\rfloor},l=0,1,\ldots,2^{-\lfloor j/2\rfloor}-1$, where $\lfloor j/2\rfloor$ is the integer part of $j/2$; and 3) translation $\boldsymbol{S}=(s_1,s_2)\in\mathbb{Z}^2$.

The curvelet transform formulation operates hierarchically, capturing signal features at diverse scales and orientations. Commencing with downsampling, the input signal progressively

undergoes subsampling to yield different scales. At each scale j, the signal transforms across distinct directions θ_l using specialized operators $\boldsymbol{R}_{\theta_l}$. The resultant transformed coefficients are then further translated by $\boldsymbol{S}$ to account for local shifts in the signal.

The curvelet function is mathematically defined as

$$\psi_{j,l,\boldsymbol{S}}(t,x)=\psi_j\left(\boldsymbol{R}_{\theta_l}\left((t,x)-P_{j,l,\boldsymbol{S}}\right)\right) \tag{10}$$

where $P_{j,l,\boldsymbol{S}}$ represents the position of the curvelet, determined through a fusion of rotation and shift:

$$P_{j,l,\boldsymbol{S}}=\boldsymbol{R}_{\theta_l}^{-1}\left(s_1\cdot 2^{-j},s_2\cdot 2^{-\lceil j/2\rceil}\right), \tag{11}$$

and $\boldsymbol{R}_{\theta_l}$ signifies the rotation matrix with angle θ_l, given by

$$\boldsymbol{R}_{\theta_l}=\begin{pmatrix}\cos\theta_l & \sin\theta_l\\ -\sin\theta & \cos\theta_l\end{pmatrix} \tag{12}$$

The curvelet function ψ_j in Eq. (10) is the formulated through the Fourier transform U_j, defining a window in frequency domain:

$$U_j(r,\theta)=2^{-3j/4}V_r\left(2^{-j}r\right)V_\Omega\left(\frac{2^{\lfloor j/2\rfloor}\theta}{2\pi}\right). \tag{13}$$

The support of U_j corresponds to a polar "wedge", shaped by the support of $V_r(r)$ and $V_\Omega(\theta)$. These radial and angular windows incorporate scale-dependent window widths for each direction, forming a wedge-like structure as illustrated in Fig. 6(a). Adhering to admissibility conditions, V_r taking positive value arguments and is supported on $r\in(-1/2,1/2)$, while V_Ω taking real arguments and supported on $\Omega\in[-1,1]$:

$$\sum_{j=-\infty}^{\infty}V_r^2\left(2^j r\right)=1, r\in(3/4,3/2) \tag{14}$$

$$\sum_{j=-\infty}^{\infty}V_\Omega^2(\Omega-j)=1,\Omega\in(-1/2,1/2) \tag{15}$$

The curvelet transform occurs within the f-k plane, yielding corresponding curvelet coefficients:

$$c_{j,l,\boldsymbol{S}}=\frac{1}{(2\pi)^2}\iint\widehat{\boldsymbol{D}}(f,k)U_j(\boldsymbol{R}_{\theta_l}(f,k))e^{i\langle P_{j,l,\boldsymbol{S}},(f,k)\rangle}\mathrm{d}f\mathrm{d}k, \tag{16}$$

where the $\langle\,\rangle$ denotes the inner product. Detailed implementation can be found in Candès et al. (2006).

2.3. Process workflow

Combining VMD and the curvelet transform, the proposed extraction method is depicted through Algorithm 2. This approach is applied to the COGs of the measured waveform $\boldsymbol{W}(o,t,x)\in\mathbb{R}^{O\times M\times N}$, where O denotes the number of offsets (receivers). Fig. 1 provides an overview of the workflow on a single COG $\boldsymbol{D}(t,x)$.

The initial step involves VMD operating on a single-channel spatial signal $d(x)$, derived by slicing the COG in the spatial domain. VMD separates this signal into two modes. The low-wavenumber IMF, only containing the direct flexure waves, is then subtracted from the input COG.

Subsequently, the VMD-filtered outcomes undergo multi-scale and multi-directional representation using the curvelet transform. The curvelet coefficients are initially subject to a hard thresholding operation:

$$c_{j,l,\boldsymbol{S}}=\begin{cases}1 & c_{j,l,\boldsymbol{S}}\le\beta\max(c)\\ 0 & c_{j,l,\boldsymbol{S}}>\beta\max(c)\end{cases} \tag{17}$$

Given that the amplitude of the direct waves typically surpasses that of the reflected waves, it proves beneficial to eliminate the larger coefficients, determined by a proportion β of the maximum value of the curvelet coefficient.

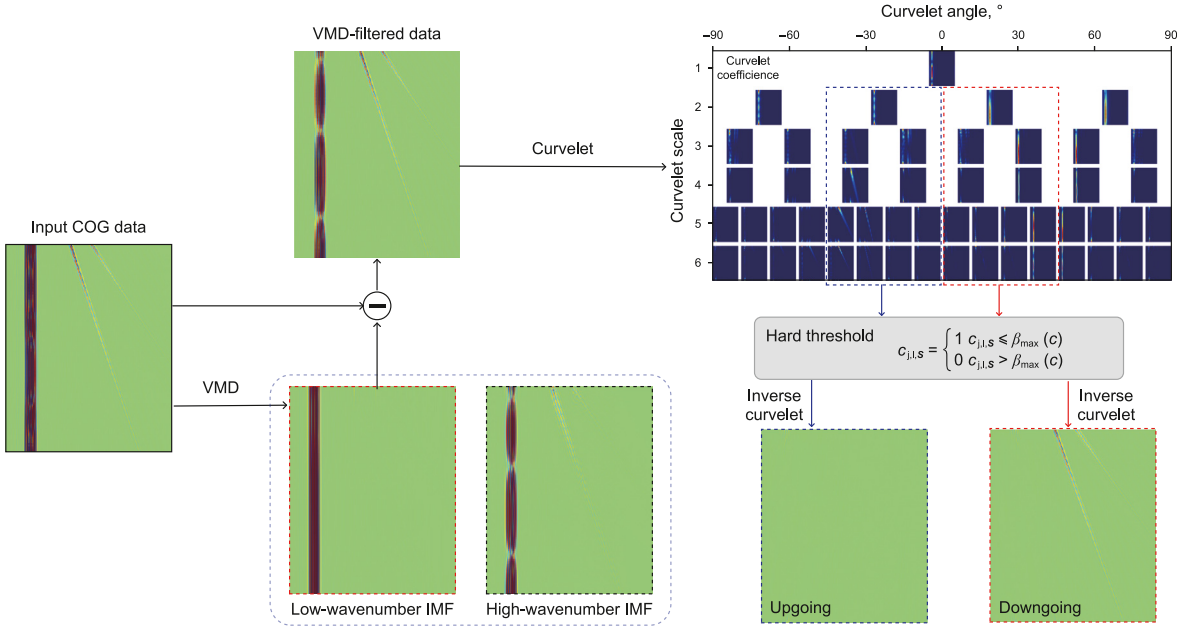

Fig. 1. Overall workflow for processing a single COG data.

Algorithm 2. Proposed extraction method

Require: $\boldsymbol{W}(o,t,x) \in \mathbb{R}^{O\times M\times N}$, β

for $i^o = 1{:}O$ **do**

Extract COG: $\boldsymbol{D}(t,x) \leftarrow \boldsymbol{W}(o=i^o,t,x)$

for $i^t = 1{:}M$ **do**

Slice 1D spatial signal: $d(x) \leftarrow \boldsymbol{D}(t=i^t,x)$

Perform VMD: IMF_1,$\mathrm{IMF}_2 \leftarrow VMD\big(d(x)\big)$ using Algorithm 1

Remove direct waves: $\boldsymbol{D}(t=i^t,x) \leftarrow \boldsymbol{D}(t=i^t,x) - \mathrm{IMF}_1$, where IMF_1 denotes the low-wavenumber mode.

end for

Compute curvelet coefficients: $c_{j,l,\boldsymbol{s}}$ using Eq. (16)

Update curvelet coefficients: $c_{j,l,\boldsymbol{s}}$ using hard threshold in Eq. (17)

Select curvelet coefficients: $c^{\mathrm{up}}_{j,l,\boldsymbol{s}}, c^{\mathrm{down}}_{j,l,\boldsymbol{s}}$ using the strategy in Eq. (18)

Obtain upgoing and downgoing reflected COG: $\boldsymbol{D}^{\mathrm{up}}(t,x), \boldsymbol{D}^{\mathrm{down}}(t,x)$ using the inverse curvelet transform.

end for

Recomposite the COGs: $\boldsymbol{W}^{\mathrm{up}}(o,t,x) = \left[\boldsymbol{D}^{\mathrm{up}}_{o=1}(t,x),\ldots,\boldsymbol{D}^{\mathrm{up}}_{o=O}(t,x)\right]$,

$$\boldsymbol{W}^{\mathrm{down}}(o,t,x) = \left[\boldsymbol{D}^{\mathrm{down}}_{o=1}(t,x),\ldots,\boldsymbol{D}^{\mathrm{down}}_{o=O}(t,x)\right]$$

return Upgoing and downgoing reflected waves: $\boldsymbol{W}^{\mathrm{up}}(o,t,x), \boldsymbol{W}^{\mathrm{down}}(o,t,x)$

Finally, coefficients corresponding to upgoing and downgoing reflected waves are selected based on their scale and angle:

$$c_{j,l,\boldsymbol{s}} \in \begin{cases} \text{upgoing}, & j>1 \quad and \quad -45^\circ < l < 0 \\ \text{downgoing}, & j>1 \quad and \quad 0 < l < 45^\circ \end{cases} \tag{18}$$

The reflected waves in the space-time domain are subsequently obtained through an inverse curvelet transform of the selected coefficients. This comprehensive approach thereby successfully extracts the reflected shear waves from the dipole acoustic logging data, facilitating enhanced analysis and migration.

3. Case study

3.1. Simulation data

In the first stage of our analysis, we assess the efficacy of the proposed methodology using a synthetic dipole array waveform within a depth range of 20 m. Illustrated in Fig. 2(a), the geological model comprises two reflectors, demarcated by black lines, strategically positioned external to the borehole. Significantly, Reflector 1 and Reflector 2 form intersection angles of 15° and 30° with the borehole, respectively. The separation between receiver R and the intersection points A_1 and A_2 is 15 m and 10 m, respectively. Comprehensive details regarding the properties of the formation and borehole are enumerated in Table 1. Both reflectors share a consistent shear stiffness of 500 GPa/m.

The experimental configuration features an array of 8 receivers meticulously situated 3.6 m above the dipole source, denoted by T, with a receiver spacing of 0.1524 m. Emitting a Ricker wavelet at a central frequency of 3 kHz, the dipole source's response is observed over a spatial depth interval of 0.1524 m. Both the receivers and the source are incrementally lowered to systematically cover the simulation within a 20 m depth range. The temporal sampling interval is set at 36 ms to ensure accurate characterization of the reflected wavefield dynamics.

The simulation of the reflected SH waves is conducted through the far-filed asymptotic solution and elastic reciprocity theory, with comprehensive details provided in Appendix A for reference. Fig. 3(b) depicts the COG corresponding to the first receiver, illustrating the behavior of the reflected SH waves. In this scenario, the distance between the reflectors and the acoustic logging tools

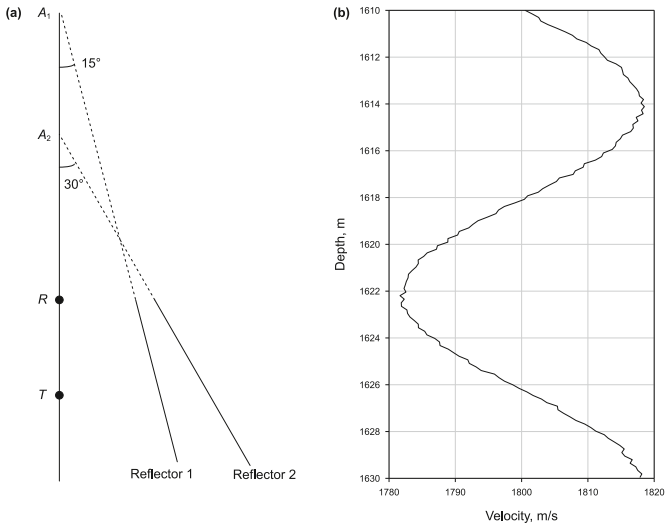

Fig. 2. Geological model **(a)** and formation S-velocity **(b)** for simulation of reflection and direct waveforms of borehole shear-wave reflection survey, respectively.

Table 1
Formation and borehole fluid parameters.

Parameter	P-velocity, m/s	S-velocity, m/s	Density, kg/m^3	Radius, m
Fluid	1500	–	1000	0.1
Formation	3500	1800	2600	∞

increases with depth, resulting in an extended propagation path for the reflected waves. Consequently, the amplitude of the reflected waves diminishes, and their arrival time is delayed. The corresponding direct waves are acquired through the discrete wavenumber integration technique (Cheng and Toksoz, 1981).

The direct mode waveform's slight depth-dependent variability displayed in Fig. 3(c), attributable to the utilization of variable S-velocity of background formation, as shown in Fig. 2(b). This introduces complexity to the task of extracting the reflected waves. The formation P-velocity and density remain constant, as detailed in Table 1. To generate the complete waveform, the reflected and direct waves are summed, as seen in Fig. 3(a). It is noteworthy that the reflected wave from reflector 2 has an extremely low amplitude, posing a challenge for visual discernment in the lower section.

Employing a 2D Fourier transform, we analyze the f-k spectrum of the composite waveform (Fig. 3(a)) and the individual direct (Fig. 3(c)) and reflected (Fig. 3(b)) waves. These spectra are presented in Fig. 3(d)–(f), respectively. The reflected waves' energy manifests as two inclined feature with different angle in Fig. 3(e). Conversely, the energy associated with the direct events predominantly clusters in the low-wavenumber region in Fig. 3(f). This disparity lays the groundwork for the f-k transform method, which capitalizes on the apparent velocity range to isolate direct events effectively. However, the significant overlap between reflected and direct energy in the f-k spectrum (Fig. 3(e)) undermines the validity of the f-k transform technique for extraction purposes.

Based on the f-k spectrum analysis presented in Fig. 3, the direct waves can potentially be extracted by filtering out the low-wavenumber components. To achieve this, the variable mode decomposition technique is employed to iteratively decompose the

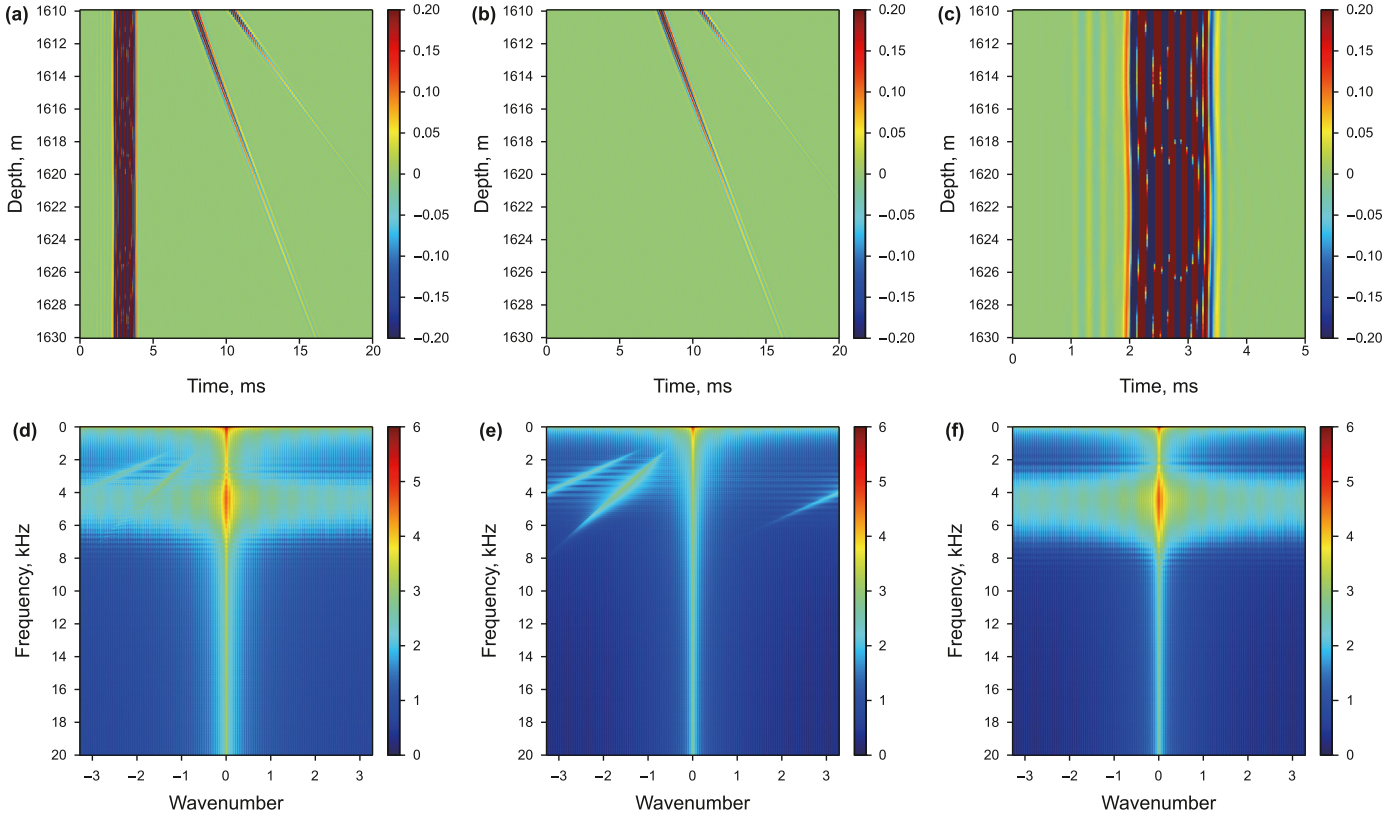

Fig. 3. Simulation waveform and f-k spectrum. **(a)** composite waveform, **(b)** reflected waveform, **(c)** direct waveform, **(d–f)** the f-k spectrum of (a–c).

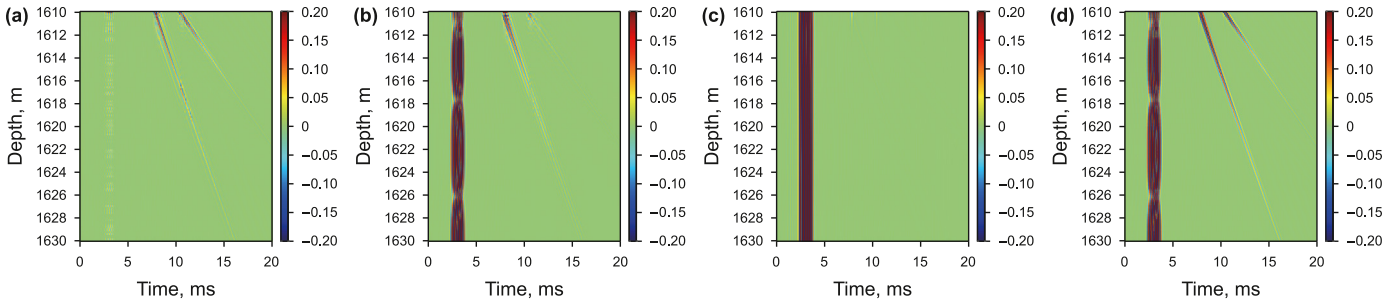

Fig. 4. Decomposed results and filtered Waveform using VMD. **(a)** Residual signals, **(b)** high-wavenumber IMF, **(c)** low-wavenumber IMF, **(d)** filtered waveform.

single-channel signal $d(x)$ in the COG $\boldsymbol{D}_o(x,t)$. The results of this decomposition are illustrated in Fig. 4.

Fig. 4(c) showcases the low-wavenumber IMF, which predominantly contains the direct waves. On the other hand, the high-wavenumber IMF displayed in Fig. 4(b) encompasses both the reflected waves and a portion of the direct waves. This coexistence is attributed to the presence of direct wave energy within the high-wavenumber zone, as depicted in Fig. 3(f). In an attempt to further isolate the direct waves, Fig. 4(a) illustrates the residual signal post VMD optimization, albeit still retaining elements of the reflected waves.

It's worth noting that the residual signal's strength could be

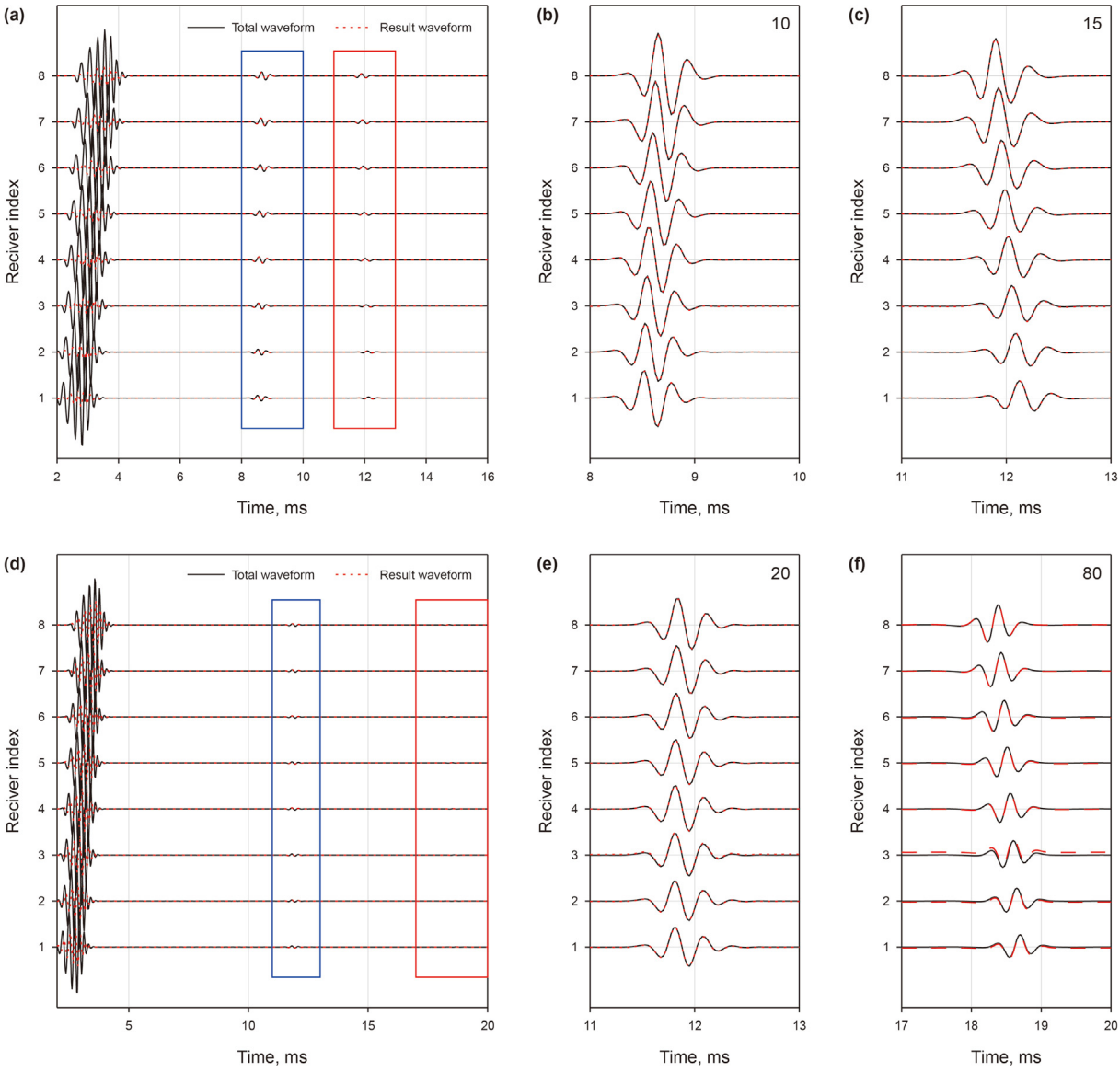

Fig. 5. Comparison between original (black line) and VMD-filtered waveform (red dotted line) at two specific depths. **(a)** 1612 m, **(b–c)** zoom in blue and red rectangle in (a), **(d)** 1620 m, **(e–f)** zoom in blue and red rectangle in (d).

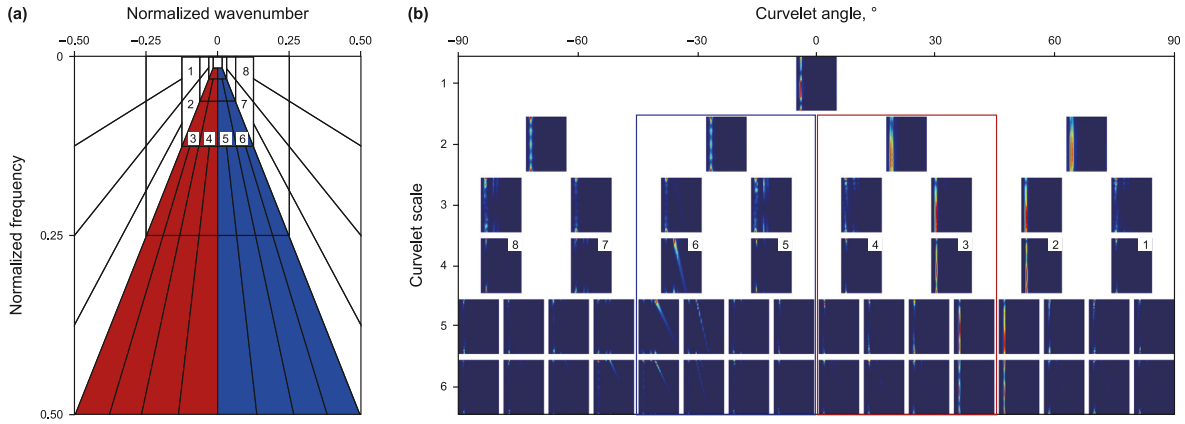

Fig. 6. Curvelet coefficients **(b)** of VMD-filtered waveform using the curvelet windows **(a)**.

minimized through meticulous adjustment of VMD's super-parameters. However, such optimization is both intricate and time-consuming. Consequently, an alternative approach is adopted wherein the filtered waveform (Fig. 4(d)) is obtained by directly subtracting the low-wavenumber IMF from the total waveform. This strategy effectively preserves the entire reflected waves and sidesteps the complexities associated with fine-tuning VMD's super-parameters.

In order to further substantiate the efficacy of the filtered approach using VMD, Fig. 5 presents processing outcomes at depths 1612 m and 1620 m. In Fig. 5(a), the initial arrival corresponds to the direct waves, succeeded by the variable reflected waves observed across multiple receivers. Notably, the reflected wave exhibits a weaker amplitude compared to the direct wave, posing challenges in identifying the reflected wave from reflector 2 and complicating the extraction process. However, the filtered reflected waves (red dotted line) align seamlessly with the original reflected waves (black line) illustrated in Fig. 5(a). Fig. 5(b), (c) provide an amplified view of the filtered results (highlighted by the blue and red rectangles), revealing a complete correspondence with the original reflected waves. The filtered outcomes maintain high accuracy, even in scenarios where the reflected waves are significantly weaker than the direct waves at a depth of 1620 m, as illustrated in Fig. 5(d)–(f). It's important to note that different scaling factors are applied to amplify the reflected waves, as displayed in the corresponding figures.

To quantitatively assess the performance of VMD, the metric is defined as the ratio between the maximum amplitudes of the direct (dic) and reflected waves (ref):

$$\mathrm{RMDR} = \left(\sum_{o=1}^{O} \frac{\max(\mathrm{dic})}{\max(\mathrm{ref})} \right) \Big/ O, \tag{19}$$

where O is the number of receivers, and the direct and reflected waves are determined by the selected time windows. It's important to note that this ratio represents the average across 8 receivers. For Fig. 5(a), the time interval selected for the direct and reflected waves ranges from 1.5 to 4 ms and from 8 to 13 ms, respectively. The RMDR of the original waveform and the VMD-filtered waveform equates to 13.9 and 2.79, respectively. Using the reflected time range of 11–20 ms, the RMDR value is 40.8 and 18.7 for Fig. 5(d).

To further eliminate the direct waves component, the filtered waveform from Fig. 4(d) is subjected to the curvelet transform. The resulting curvelet panels are showcased in Fig. 6(b). The frequency-wavenumber partitioning strategy employed by the curvelet transform is depicted in Fig. 6(a). The curvelet transformation incorporates 6 scales, visually represented by co-centered squares. Given that the analyzed COG is based on real data, only half of the f-k plane is significant. The first scale (Scale 1) is the coarsest and lacks directional attributes. Using Eq. (18), the subsequent scales are subdivided into smaller windows, each representing a distinct direction. Notably, in Fig. 6(a), eight curvelet windows corresponding to various directions are highlighted for Scale 4. These directions are further visualized in Fig. 6(b).

For the sake of visual coherence and uniformity, we upsample and downsample the curvelet coefficients within each individual scale and direction patch, rendering them to a uniform size of 50 × 50 pixels, similar to the approach in previous work (Naghizadeh and Sacchi, 2018). In the resultant curvelet panels, coefficients

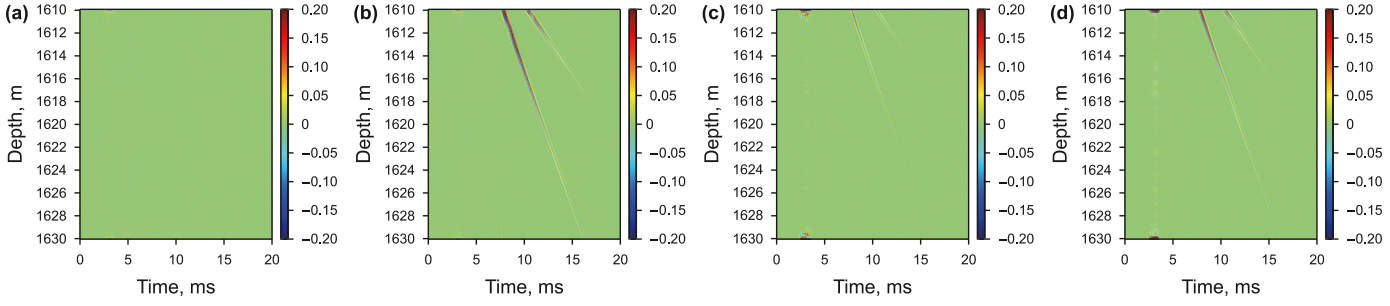

Fig. 7. Extracted upgoing **(a)** and downgoing **(b)** reflected waveform via the proposed method, and extracted results from f-k transform **(c)** and shearlet transform **(d)**.

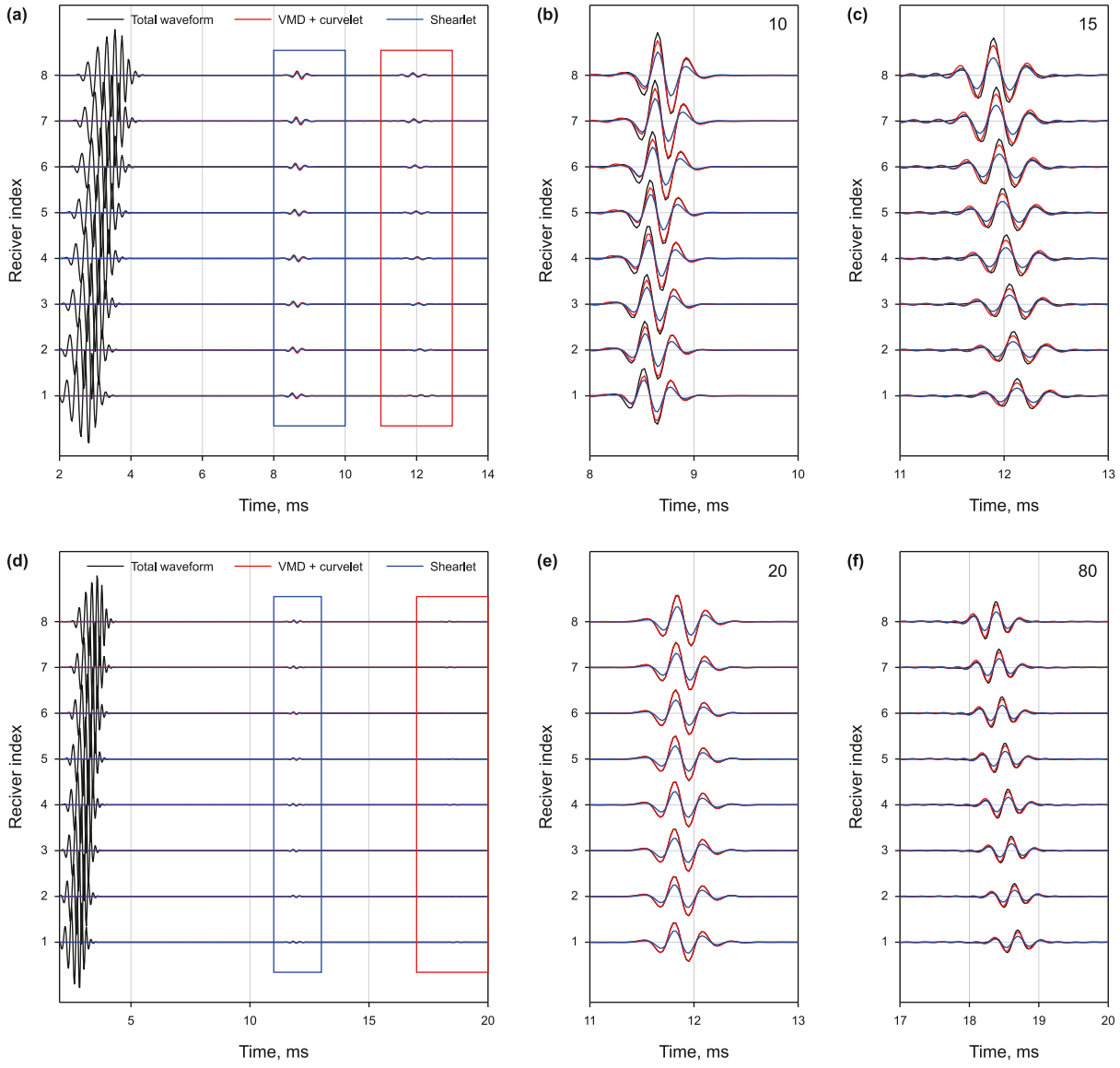

Fig. 8. Extraction reflected waveform at two specific depths. **(a)** 1612 m, **(b–c)** zoom of blue and red rectangle in (a), **(d)** 1620 m, **(e–f)** zoom of blue and red rectangle in (d). Black line represents the original waveform; red line represents extracted results of the proposed method; blue dotted line represents extracted results of the shearlet transform.

associated with the reflected waves exhibit a relatively weaker magnitude compared to those of the direct waves. To effectively mitigate the influence of highly intense direct waves, we employ a hard threshold (Eq. (17)) with a threshold value of $\beta =$ 0.9. Remarkably, the curvelet panels encompassing the $-45°$ angle range at scales 2–6 (indicated by the blue rectangle) distinctly feature the downgoing reflected waves. This observation validates the appropriateness of the selection strategy detailed in Eq. (18). Specifically, the correlation between the blue and red-colored curvelet windows corresponds well with the strategy's predictions. On the contrary, panels within the red rectangle predominantly capture direct waves. This distinction arises because the synthetic data utilized for this study lack upgoing reflected waves.

Fig. 7 showcases a comparison between the outcomes of the proposed extraction method, the f-k transform and the shearlet transform method. The extracted upgoing waveforms are displayed in Fig. 7(a), where no reflected event is observed, attributed to the absence of upgoing waveforms in the simulated data presented in Fig. 3(b). In Fig. 7(b), the downgoing reflected waveform is depicted, demonstrating a significant intensity relative to the residual direct waveform. It is worth noting that the strength of reflected waves in Fig. 7(b) facilitates accurate migration, subsequently enabling precise imaging of reflectors. Moreover, the residual direct waveform might persist as noise in the migration image. Techniques for noise removal within migration images have been explored in previous studies (Kong et al., 2023).

Employing the identical hard threshold approach as presented in Chen et al. (2019), the outcomes of the shearlet transform are portrayed in Fig. 7(d). For extracting reflected waves, the parameters are set as $s \neq 0$ and $a = 0, 1/4, 1/16$ in the paper. While effectively removing the strong direct mode waves, a slight attenuation is observed in the reflected waves. This attenuation, though subtle, surpasses the performance of the f-k transform shown in Fig. 7(c), consistent with the findings of Chen et al. (2019). This nuanced attenuation emphasizes the comparative robustness of the proposed method in accurately preserving the reflected wave component.

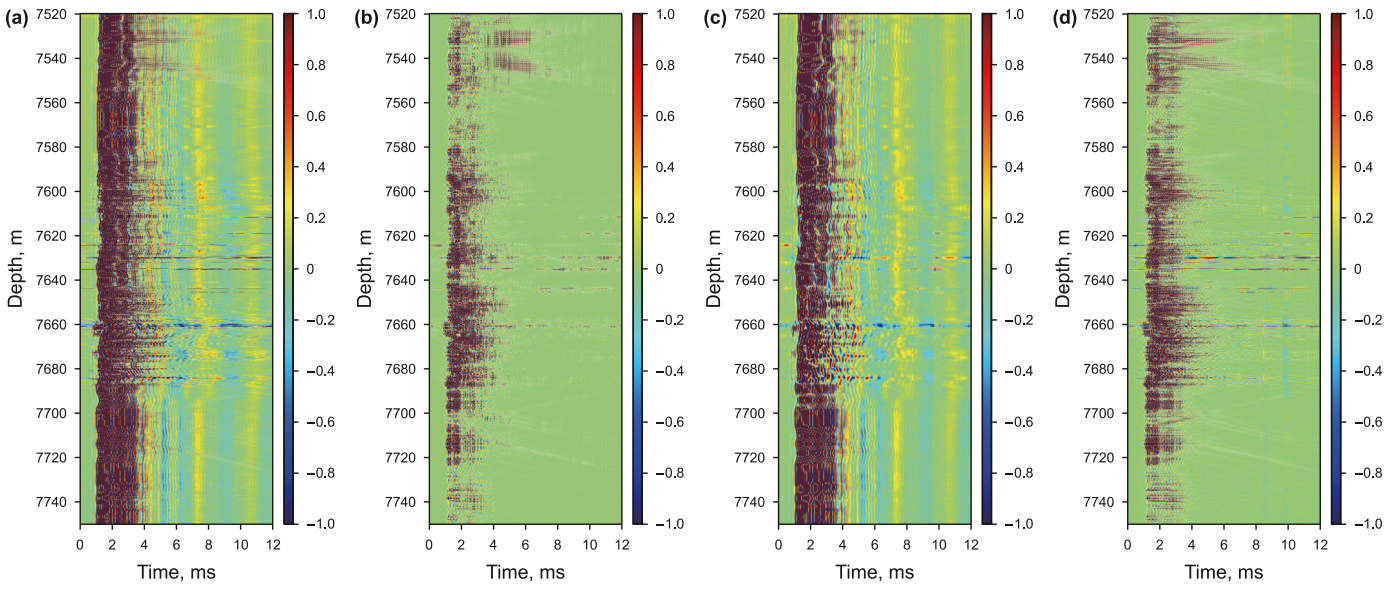

Fig. 9. Decomposed IMFs **(b, c)** and filtered waveform **(d)** of measured field waveform in an open-hole well **(a)** using VMD.

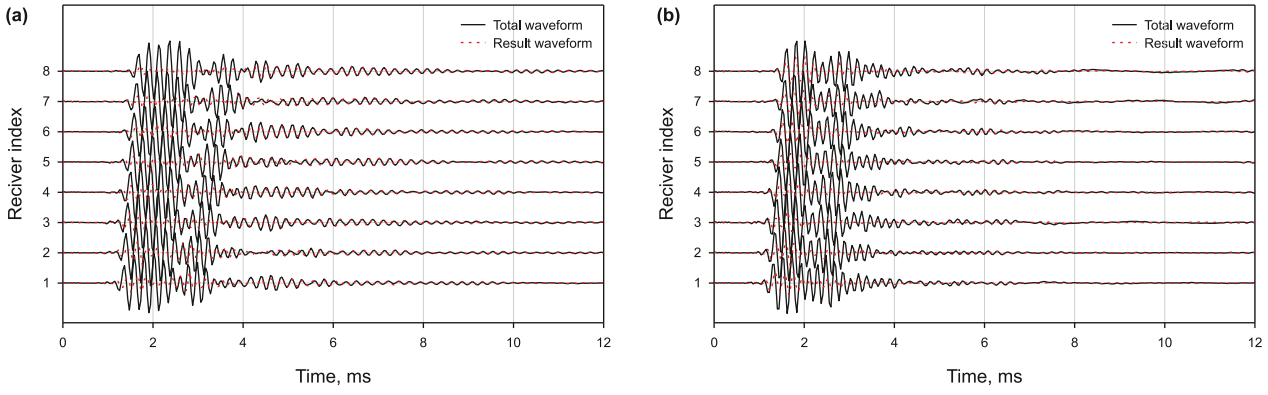

Fig. 10. Comparison between original and VMD-filtered waveform at two specific depths. **(a)** 7544 m, **(b)** 7717 m.

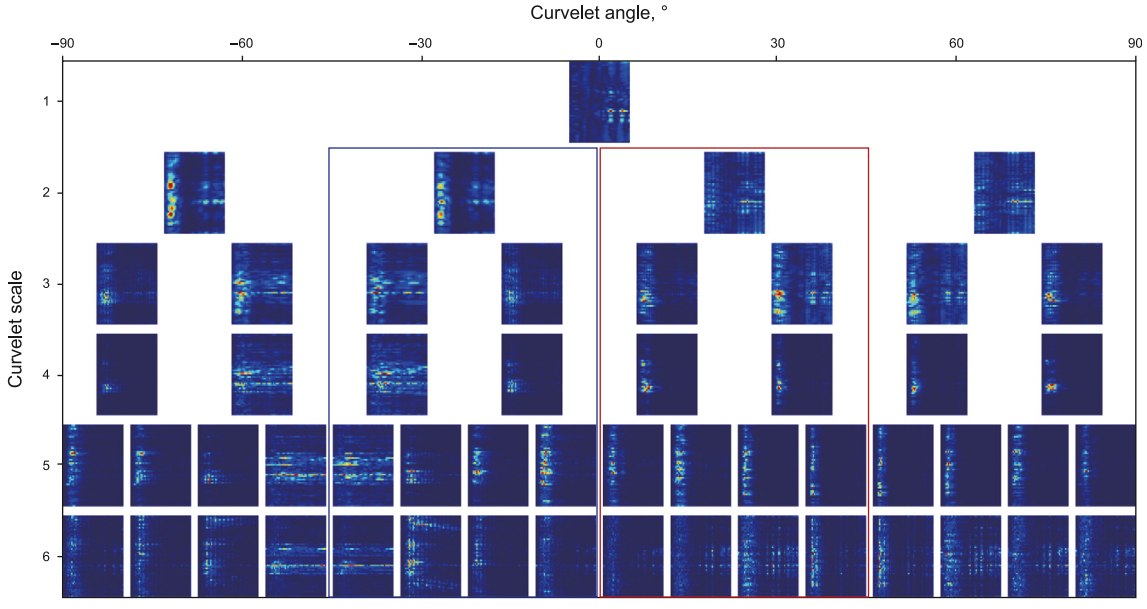

Fig. 11. Curvelet coefficients of VMD-filtered waveform.

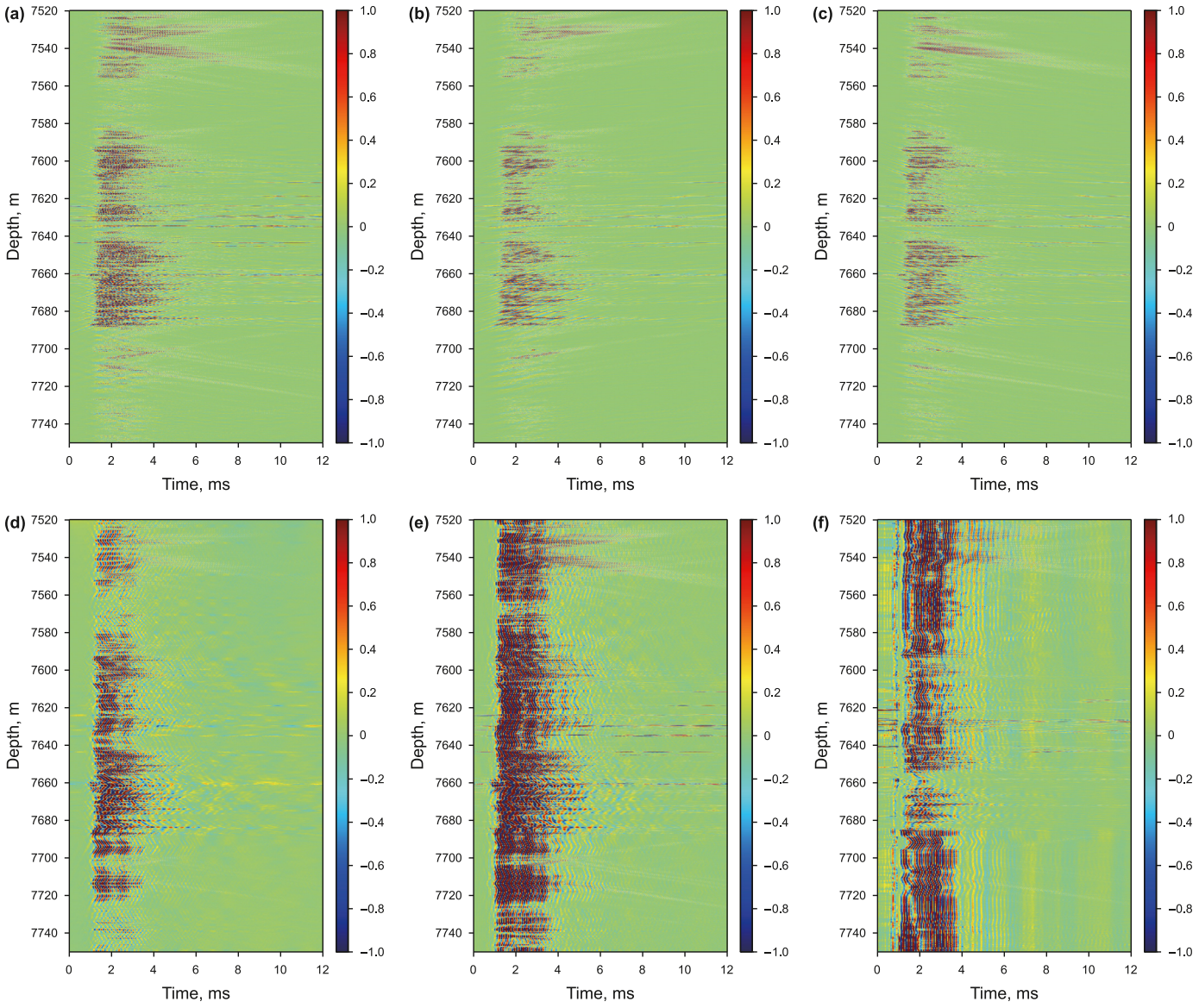

Fig. 12. Combined reflected waveforms extracted using the proposed method **(a)**, f-k transform **(d)**, shearlet transform **(e)**, and parameter prediction **(f)**. Additionally, the upgoing and downgoing reflected waveforms separated using the proposed method are shown in **(b)** and **(c)**, respectively.

To offer a more detailed perspective on the processing results, Fig. 8 delineates the array waveform at the same depth as Fig. 5. In Fig. 8(a), (d), the direct waves are successfully eliminated in comparison to the results presented in Fig. 5(a), (d), where only VMD was employed. Nonetheless, the reflected waves are effectively preserved and closely aligned with the original reflected waves. In contrast to Fig. 8(b) and (f) exhibits a more significant error in the results of shearlet transform, where the reflected wave is notably decreased. Conversely, the extracted results of the proposed method consistently overlay with the original reflected waves. The calculated RMDR, using the same time range for both curvelet transform and shearlet transform, yields values of (0.04, 0.06) and (0.06, 0.6), respectively. This quantification further demonstrates the superior performance of the proposed method over the shearlet transform.

3.2. Field data

In the context of the field example, we employ a dipole waveform gathered from carbonate reservoir in Tarim Basin in China, as depicted in Fig. 9(a). The measurement is conducted in an open-hole horizontal well, where two distinct formation boundary reflected waves emerge within the depth intervals of 7520–7550 m and 7700–7730 m, albeit overshadowed by the presence of substantial direct wave interference.

To address this issue, we first employ the variational mode decomposition technique. Through VMD, we decompose the waveform into high-wavenumber and low-wavenumber IMFs, as showcased in Fig. 9(b), (c), respectively. Much akin to the synthetic instances illustrated in Fig. 4(b), it is apparent that Fig. 9(c) predominantly captures the direct waves component. Subtraction of Fig. 9(c) from the original waveform (Fig. 9(a)) results in the filtered waveform depicted in Fig. 9(d). This transformation significantly suppresses the direct waves' presence, thereby preserving the integrity of the reflected waves.

Fig. 10 provides a granular view of the filtered array waveform at depths of 7544 and 7717 m, respectively. Notably, the reflected waves remain intact, while the first arrival of the direct waves is

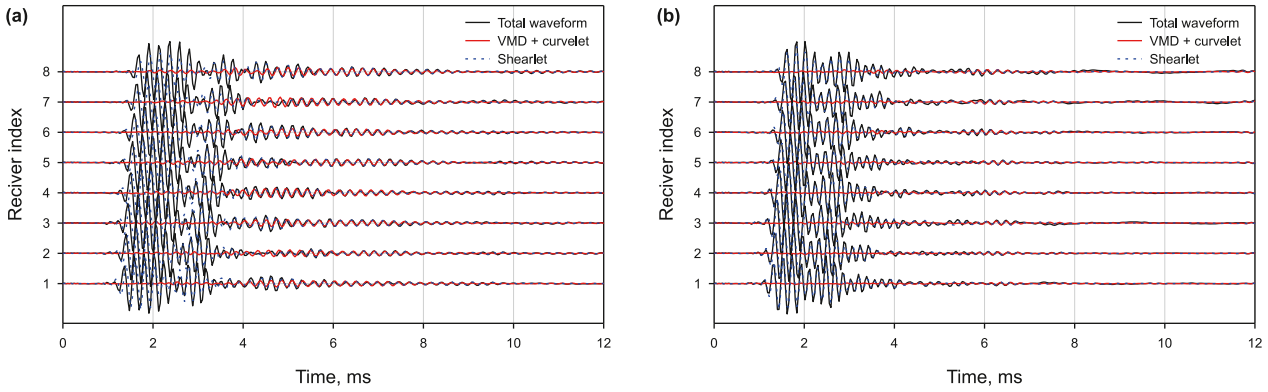

Fig. 13. Extraction reflected waveform at two specific depths: **(a)** 7544 m, **(b)** 7717 m.

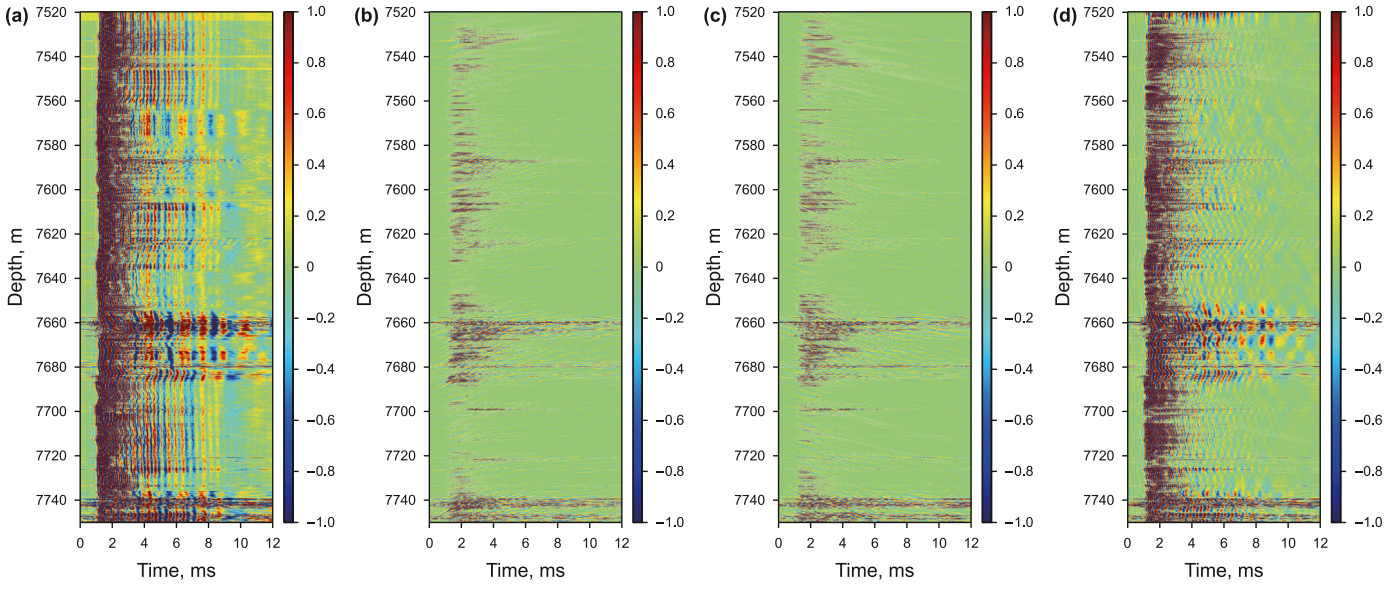

Fig. 14. Extracted reflected waveform via the proposed method and shearlet transform. **(a)** Measured waveform after casing; **(b)** upgoing reflected waveform; **(c)** downgoing reflected waveform; **(d)** extracted results via shearlet transform.

substantially mitigated. Quantitatively, the RMDR diminish from 6.34 to 2.21 in Fig. 10(a) and from 11.32 to 6.30 in Fig. 10(b) after VMD filtering, underlining the efficacy of this approach.

The curvelet panels showcased in Fig. 11 further corroborate these findings. Here, it is evident that the curvelet coefficients corresponding to reflected waves are significantly smaller than those attributable to direct mode waves. The threshold value β is set as 0.5. Consequently, the utilization of selected curvelet panels, guided by Eq. (18) and delineated by the blue and red rectangles in Fig. 11, facilitates the separation of upgoing and downgoing reflected waves from the comprehensive waveform.

In Fig. 12(b), (c), the isolated upgoing and downgoing reflected waveforms are presented, respectively. The combined outcomes in Fig. 12(a) validate the successful attenuation of prominent direct mode waves while simultaneously preserving the integrity of the reflected waves. Notably, the proposed method exhibits superior direct wave suppression compared to the shearlet transform results illustrated in Fig. 12(e). This observation is particularly discernible in the mitigation of direct wave leakage, a phenomenon evident in the shearlet transform outputs. A comparative analysis with the f-k transform in Fig. 12(d) reveals that the proposed method adeptly retains useful reflected waves, thereby outperforming the f-k transform which inadvertently removes a portion of these valuable reflections. To provide additional validation for the efficacy of the proposed method, Fig. 12(f) showcases the processed results of the parameter prediction method (Tang, 1997). This model-based approach critically depends on a predefined velocity model and successfully diminishes direct mode waves in the depth interval of 7650–7680 m. Nevertheless, it falls short in effectively removing direct waves in the target interval encompassing the reflected waves when compared to the processing outcomes depicted in Fig. 12(a).

Fig. 13 extends this analysis to two specific depth points (7544 m and 7717 m). Within the temporal interval of 0.5–4 ms, the direct waves are effectively attenuated through the employment of both the curvelet and shearlet transforms. Meanwhile, the subsequent reflected waves, occurring after 4 ms, are notably preserved. In terms of quantitative assessment, the RMDR metrics for the shearlet transform results in Fig. 13(a), (b) yield values of 1.52 and 2.93, respectively. In contrast, the corresponding RMDR values for the proposed method are 0.72 and 0.76, both of which are less than 1. This discrepancy underscores a crucial observation: the proposed method engenders reflected waves that exhibit superior strength in comparison to the direct waves.

To provide further substantiation for the validity of the processing outcomes, we conducted analysis on the acquired waveform from the same well following casing. The findings are showcased in Fig. 14. Similarly, the reflected waves in this scenario are tainted by direct wave interference. Leveraging the proposed approach that amalgamates the VMD and curvelet transform, the retrieved reflected waveforms are illustrated in Fig. 14(b), (c). Notably, these results align closely with the outcomes depicted in Fig. 12(a), (b), respectively. Significant measured noise, stemming from the intricate borehole environment, is notably present at various depths, including 7740, 7660, and 7680 m. This contributes to the observed disparities in waveforms before (Fig. 12) and after (Fig. 14) casing. It is crucial to emphasize that our analytical and extraction efforts are concentrated on specific depth sections, specifically 7520–7550 m and 7700–7730 m. In these sections, the influence of measured noise is minimized, enabling a more precise evaluation of the extracted reflected waves. In stark contrast, the outcomes from the shearlet transform fail to meet the criteria of acceptability due to the pronounced presence of residual direct waves. Collectively, these field-based instances provide compelling evidence attesting to the efficacy and resilience of the proposed method in practical acoustic logging data processing scenarios.

4. Conclusion

The accurate extraction of reflected waves holds paramount importance in the realm of borehole acoustic reflection imaging technology, as the quality of the extracted results profoundly impacts the ensuing image quality. This paper introduces a novel methodology for the extraction of reflected waves, achieved through a sequential application of variational mode decomposition and curvelet transform techniques. This approach facilitates the simultaneous separation of upgoing and downgoing reflected waves. The VMD process involves the iterative decomposition of common offset gather data from the full array waveform in the 1D depth domain, yielding high and low wavenumber IMFs. Subsequently, the low-wavenumber IMF, containing the direct mode waves, is subtracted from the full waveform, thereby preserving the reflected waves. The resultant waveform is then subjected to Curvelet transform, wherein the direct waves are further removed using hard thresholding. The extraction of upgoing and downgoing reflected waves is facilitated based on the selection of appropriate scales and angles in the curvelet domain. Application of this approach to synthetic and field data yields compelling results: the direct mode waves are significantly attenuated, while the reflected waves remain intact. Importantly, the proposed method substantially enhances the ratio between the maximum values of direct and reflected waves, surpassing the efficacy of the shearlet transform approach. This verifies the potency of the VMD and curvelet transform combination in weak reflect event extraction.

CRediT authorship contribution statement

Fan-Tong Kong: Writing – review & editing, Writing – original draft, Visualization, Supervision, Methodology. **Yong-Xiang Liu:** Visualization, Methodology, Data curation. **Xi-Hao Gu:** Visualization, Software. **Li Zhen:** Funding acquisition, Data curation. **Cheng-Ming Luo:** Writing – original draft, Investigation, Conceptualization. **Sheng-Qing Li:** Writing – review & editing, Supervision, Funding acquisition.

Declaration of competing interest

The authors declare that they have no known competing financial interests or personal relationships that could have appeared to influence the work reported in this paper.

Acknowledgement

The authors express their gratitude to Emmanuel Candès, Laurent Demanet, David Donoho, and Le-Xing Ying, Curvelab, for providing access to their curvelet transform toolbox (http://www.curvelet.org/index.html). This work was supported by the National Natural Science Foundation of China (grant No. 42204126, 42174145, 42104132); Laoshan National Laboratory Science and Technology Innovation Project (grant No. LSKJ202203407).

Appendix A

The geological model, illustrated in Fig. A1, encompasses a borehole configuration with an 8-receiver logging tool positioned centrally within a fluid-filled borehole. The received wavefield $RWV(\omega)$ for a single-well shear reflection survey is expressed in the frequency domain as a convolution of several factors (Tang and Patterson, 2009):

$$RWV(\omega) = S(\omega) \cdot RD(\omega) \cdot RF(\omega) \cdot RC(\omega) \frac{e^{i\omega D/\beta}}{D} e^{-\frac{\omega D}{2Q\beta\beta}}, \tag{20}$$

where $S(\omega)$ signifies the source spectrum, $RD(\omega)$ represents the borehole radiation pattern, illustrating the influence of source radiation propagating from the borehole into the formation. The borehole reception pattern $RC(\omega)$ delineates the response of the borehole to the reflection waves returning to the borehole. $RF(\omega)$ defines the reflectivity at the reflector. The propagation loss encompasses two crucial components: geometric spreading ($1/D$, where D signifies the total distance traveled to and from the reflector) and amplitude attenuation ($e^{-(\omega D)/(2Q_\beta\beta)}$, where Q_β and β denote the shear-wave quality factor and velocity, respectively). It is noteworthy that all factors listed above exhibit frequency-dependent variations.

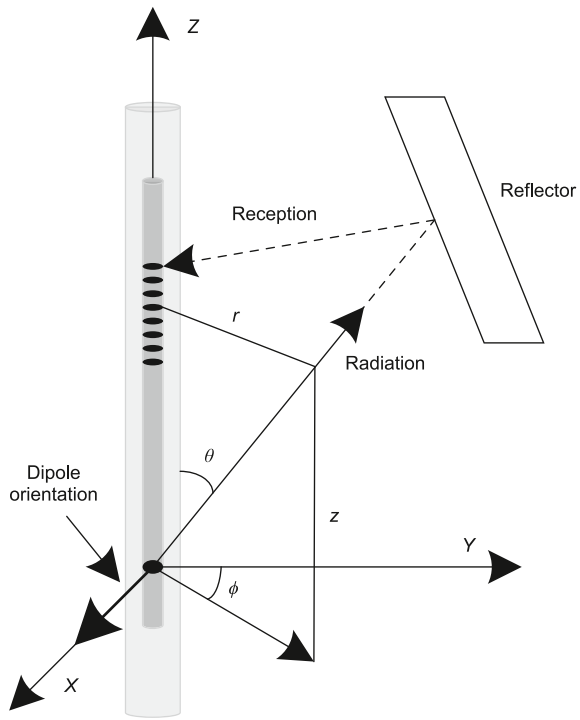

Fig. A1. Borehole model and coordinates system for simulating the single well shear reflection survey.

The far-filed asymptotic solution method is employed for the

rapid calculation of the borehole radiation pattern $RD(\omega)$ (Tang et al., 2014). The SH-wave displacement potentials corresponding to a dipole source are described by the wave-number integrals (Tang and Patterson, 2009):

$$\chi(\omega; r, z) = \frac{S(\omega)\cos\varphi}{4\pi}\int_{-\infty}^{+\infty} D(\omega, k)K_1(sr)\mathrm{e}^{ikz}\mathrm{d}k \tag{21}$$

where $K_1(sr)$ is modified Bessel function, and the coefficient $D(\omega, k)$ could be determined using discrete wavenumber integration method (Cheng and Toksoz, 1981). A steepest descent method can be applied to obtain the far-field asymptotic solution for displacement potentials in Eq. (21). This is because the radiation waves penetrate deep into the formation and reflection occurs in the far-field of the source. The new solution can be formulated as

$$\chi \sim \cos\varphi D(\omega, k_0)\frac{\mathrm{e}^{i\omega R/\beta}}{4\pi R}S(\omega), \tag{22}$$

where $k_0 = \omega\cos\theta/\beta$ is the steepest descent solution for the axial wavenumber k.

The far-field SH-wave, polarizing in the φ direction, has displacement components as follows:

$$u_\varphi \sim [i\rho\beta\omega D(\omega, k_0)\sin\theta\cos\varphi]\frac{\mathrm{e}^{i\omega R/\beta}}{4\pi\mu R}S(\omega) \tag{23}$$

where ρ and μ are formation density and shear modulus, respectively.

The dimensionless expressions for radiation pattern of SH-wave determined based on Eq. (23) are

$$RD_{\mathrm{SH}}(\omega; \theta, \varphi) = i\rho\beta\omega D(\omega, k_0)\sin\theta\cos\varphi. \tag{24}$$

Using the elastic reciprocity theorem to the borehole radiation and reception scenario (Xu and Hu, 2020; Gu et al., 2023), the reception pattern could be obtained:

$$RC_{\mathrm{SH}}(\omega, \theta) = RD_{\mathrm{SH}}(\omega, \theta). \tag{25}$$

Subsequently, regarding the reflector as a linear slip interface, the shear displacement on both sides of the interface are discontinuous because of the presence of the reflector, causing a misalignment between the media on both sides under shear stress. According to (Gu et al., 2020; Jiang et al., 2019), the corresponding reflectivity for SH-wave $RF(\omega)$ could be defined as

$$RF(\omega, \psi, \eta_{\mathrm{T}}) = \frac{(Z_1 - Z_2)\eta_{\mathrm{T}} - i\omega Z_1 Z_2\cos\psi}{(Z_1 + Z_2)\eta_{\mathrm{T}} - i\omega Z_1 Z_2\cos\psi} \tag{26}$$

where $Z_i = \rho_i\beta_i\ (i = 1, 2)$ is the formation acoustic impedance on both sides of the reflector. Here, ψ denotes the wave reflection angle onto the reflector, and η_{T} represents the shear stiffness, which is set as 500 GPa/m. In the paper, the acoustic impedance of both sides of the reflector are set as $Z = Z_1 = Z_2$, the reflectivity in Eq. (26) is simplified as

$$RF(\omega, \psi, \eta_{\mathrm{T}}) = \frac{i\omega Z\cos\psi}{i\omega Z\cos\psi - 2\eta_{\mathrm{T}}} \tag{27}$$

Finally, given a specific source spectrum, the spectrum of borehole reflection waves can be computed using Eq. (20). Performing a Fourier transform on this spectrum yields synthetic waveforms, facilitating the simulation of reflection wave data as acquired in a borehole shear-wave reflection survey.

References

Candès, E., Demanet, L., Donoho, D., Ying, L., 2006. Fast discrete curvelet transforms. Multiscale Model. Simul. 5 (3), 861–899. https://doi.org/10.1137/05064182X.

Che, X., Qiao, W., Wang, R., Zhao, Y., 2014. Numerical simulation of an acoustic field generated by a phased arc array in a fluid-filled cased borehole. Petrol. Sci. 11, 385–390. https://doi.org/10.1007/s12182-014-0352-3.

Chen, J., Yue, W., Li, C., Zeng, F., 2019. Extracting reflected waves from acoustic logging data based on the shearlet transform. Geosci. Rem. Sens. Lett. IEEE 16 (11), 1688–1692. https://doi.org/10.1109/lgrs.2019.2908286.

Cheng, C.H., Toksoz, M.N., 1981. Elastic wave propagation in a fluid-filled borehole and synthetic acoustic logs. Geophysics 46 (7), 1042–1053. https://doi.org/10.1190/1.1441242.

Cheng, L., Che, X.H., Qiao, W.X., Zhao, T., 2023. 3D trajectory inversion of an adjacent well using scattered P-wave. Petrol. Sci. 20, 857–865. https://doi.org/10.1016/j.petsci.2023.02.024.

Dragomiretskiy, K., Zosso, D., 2014. Variational mode decomposition. IEEE Trans. Signal Process. 62 (3), 531–544. https://doi.org/10.1109/TSP.2013.2288675.

Gu, X., Tang, X., Zhuang, C., Jiang, C., Li, S., 2020. Simulation of dipole shear-wave reflection survey for multi-fracture system using liner slip interface theory. Prog. Geophys. 35 (3), 955–962. https://doi.org/10.6038/pg2020DD0053 (in Chinese).

Gu, X.H., Tang, X.M., Su, Y.D., 2021. Delineating a cased borehole in unconsolidated formations using dipole acoustic data from a nearby well. Geophysics 86 (5), D139–D147. https://doi.org/10.1190/geo2020-0570.1.

Gu, X.H., Tang, X.M., Su, Y.D., Li, S.Q., 2023. Elastic wave radiation and reception of a borehole dipole source in a vertically transverse isotropic formation. Geophysics 88 (2), D177–D191. https://doi.org/10.1190/geo2022-0174.1.

Hei, C., Qi, X., Li, Z., 2023. Evaluation of the downhole hydraulic fracturing using single-well shear wave scattering imaging-modeling and field applications. Waves Random Complex Media 1–13. https://doi.org/10.1080/17455030.2023.2226238.

Hirabayashi, N., Leaney, W.S., 2019. Wavefield separation for borehole acoustic reflection survey using parametric decomposition and waveform inversion. Geophysics 84 (4), D151–D159. https://doi.org/10.1190/geo2018-0330.1.

Hornby, B.E., 1989. Imaging of near-borehole structure using full-waveform sonic data. Geophysics 54 (6), 747–757. https://doi.org/10.1190/1.1442702.

Huang, N.E., Shen, Z., Long, S.R., Wu, M.C., Shih, H.H., Zheng, Q., Yen, N.C., Tung, C.C., Liu, H.H., 1998. The empirical mode decomposition and the Hilbert spectrum for nonlinear and non-stationary time series analysis. Proc. Roy. Soc. Lond. A. 454 (1971), 454903–454995. https://doi.org/10.1098/rspa.1998.0193.

Jiang, C., Chen, X.L., Su, Y.D., Tang, X.M., 2019. Cased borehole acoustic-wave propagation with varying bonding conditions: theoretical and experimental modeling. Geophysics 84 (4), D161–D169. https://doi.org/10.1190/geo2018-0798.1.

Kong, F., Xu, H., Gu, X., Luo, C., Li, S., 2023. Denoising method of borehole acoustic reflection image using convolutional neural network. Geoenergy Sci. Eng. 226, 211761. https://doi.org/10.1016/j.geoen.2023.211761.

Lee, S.Q., Tang, X.M., Su, Y.d., 2019. Shear wave imaging to determine near-borehole faults for ocean drilling exploration. Geophys. J. Int. 217 (1), 288–293. https://doi.org/10.1093/gji/ggz023.

Li, C., Yue, W., 2017. High-resolution Radon transforms for improved dipole acoustic imaging: high-resolution Radon transforms. Geophys. Prospect. 65 (2), 467–484. https://doi.org/10.1111/1365-2478.12434.

Li, Y., Zhou, R., Tang, X., Jackson, J.C., Patterson, D.J., 2002. Single-well imaging with acoustic reflection survey. In: 64th EAGE Conference & Exhibition. https://doi.org/10.3997/2214-4609-pdb.5.P141.

Li, J., Innanen, K.A., Tao, G., 2017a. Extraction of reflected events from sonic-log waveforms using the Karhunen-Loève transform. Geophysics 82 (5), D265–D277. https://doi.org/10.1190/geo2017-0031.1.

Li, J., Innanen, K.A., Tao, G., Zhang, K., Lines, L., 2017b. Wavefield simulation of 3D borehole dipole radiation. Geophysics 82 (3), D155–D169. https://doi.org/10.1190/geo2016-0145.1.

Li, Y.H., Tang, X.M., Li, H.R., Lee, S.Q., 2021. Characterizing the borehole response for single-well shear-wave reflection imaging. Geophysics 86 (1), D15–D26. https://doi.org/10.1190/geo2020-0212.1.

Li, Z., Lee, S.Q., Qi, Q., Su, Y.D., Wang, X.J., 2022. Investigation of through-casing borehole acoustic reflection imaging with a dipole source: modeling and field application. J. Nat. Gas Sci. Eng. 105, 104715. https://doi.org/10.1016/j.jngse.2022.104715.

Liu, W., Cao, S., Chen, Y., 2016. Applications of variational mode decomposition in seismic time-frequency analysis. Geophysics 81 (5), V365–V378. https://doi.org/10.1190/geo2015-0489.1.

Liu, N., Li, F., Wang, D., Gao, J., Xu, Z., 2022. Ground-roll separation and attenuation using curvelet-based multichannel variational mode decomposition. IEEE Trans. Geosci 60, 1–14. https://doi.org/10.1109/TGRS.2021.3054749.

Ma, J., Plonka, G., 2010. The curvelet transform. IEEE Signal Process. Mag. 27 (2), 118–133. https://doi.org/10.1109/MSP.2009.935453.

Naghizadeh, M., Sacchi, M., 2018. Ground-roll attenuation using curvelet down-scaling. Geophysics 83 (3), V185–V195. https://doi.org/10.1190/geo2017-0562.1.

Rockafellar, R.T., 1973. A dual approach to solving nonlinear programming problems by unconstrained optimization. Math. Program. 5 (1), 354–373. https://doi.org/10.1007/BF01580138.

Song, J., Li, Z., Wang, G., Lei, G., Yang, J., 2023. Weak seismic signal enhancement

using curvelet transform and compressive sampling. IEEE Trans. Geosci. Rem. Sens. 61, 1–11. https://doi.org/10.1109/TGRS.2023.3253930.
Starck, J.L., Candes, E., Donoho, D., 2002. The curvelet transform for image denoising. IEEE Trans. Image Process. 11 (6), 670–684. https://doi.org/10.1109/TIP.2002.1014998.
Tang, X.M., 1997. Predictive processing of array acoustic waveform data. Geophysics 62 (6), 1710–1714. https://doi.org/10.1190/1.1444270.
Tang, X.M., Patterson, D.J., 2009. Single-well S-wave imaging using multicomponent dipole acoustic-log data. Geophysics 74 (6), WCA211–WCA223. https://doi.org/10.1190/1.3227150.
Tang, X.M., Cao, J., Wei, Z., 2014. Shear-wave radiation, reception, and reciprocity of a borehole dipole source: with application to modeling of shear-wave reflection survey. Geophysics 79 (2), T43–T50. https://doi.org/10.1190/geo2013-0096.1.
Tao, G., He, F., Wang, B., Wang, H., Chen, P., 2008a. Study on 3D simulation of wave fields in acoustic reflection image logging. Sci. China, D Earth sci. 51 (2), 186–194. https://doi.org/10.1007/s11430-008-6009-6.
Tao, G., He, F., Yue, W., Chen, P., 2008b. Processing of array sonic logging data with multi-scale STC technique. Petrol. Sci. 5 (2), 238–241. https://doi.org/10.1007/s12182-008-0036-y.
Wang, H., Tao, G., Shang, X., 2015. A method to determine the strike of interface outside of borehole by monopole borehole acoustic reflections. J. Petrol. Sci. Eng. 133, 304–312. https://doi.org/10.1016/j.petrol.2015.05.025.
Wang, H., Li, N., Wang, C., Wu, H., Liu, P., Li, Y., Liu, Y., 2020. Responses of dipole-source reflected shear waves in acoustically slow formations. J. Geophys. Eng. 17 (1), 1–17. https://doi.org/10.1093/jge/gxz078.
Wei, Z.T., Tang, X.M., 2012. Numerical simulation of radiation, reflection, and reception of elastic waves from a borehole dipole source. Geophysics 77 (6), D253–D261. https://doi.org/10.1190/geo2012-0061.1.
Xu, J., Hu, H., 2020. Solutions of P-SV and SV-P waves in single-well imaging through reciprocity relations. Geophysics 85 (6), D245–D259. https://doi.org/10.1190/geo2019-0551.1.
Yu, S., Ma, J., 2018. Complex variational mode decomposition for slop-preserving denoising. IEEE Trans. Geosci. Rem. Sens. 56 (1), 586–597. https://doi.org/10.1109/TGRS.2017.2751642.
Zhang, G., Li, N., Guo, H.W., Wu, H.L., Luo, C., 2015. Fracture identification based on remote detection acoustic reflection logging. Appl. Geophys. 12 (4), 473–481. https://doi.org/10.1007/s11770-015-0522-0.